Temporal Localized Turing Patterns in Vertical External-Cavity Surface-Emitting Laser

Adrian Bartolo
Université Côte d'Azur
Nathan Vigne
Institut d'Electronique et des Systèmes
Mathias Marconi
Université Côte d'Azur
Grégoire Beaudoin
CNRS
Konstantinos Pantzas
Centre de Nanosciences et de Nanotechnologies https://orcid.org/0000-0002-2297-3247
Isabelle Sagnes
Centre de Nanosciences et de Nanotechnologies, C2N UMR 9001, CNRS, Université Paris Sud, Université Paris Saclay, 91120 Palaiseau, France https://orcid.org/0000-0001-8068-6599
Guillaume Huyet
Université Côte d'Azur
Fabian Maucher
Universitat de les Illes Baleares
Svetlana Gurevich
University of Münster
Julien Javaloyes
Departament de Física, Universitat de les illes Baleares https://orcid.org/0000-0001-9131-4483
Arnaud Garnache
Institut d'Electronique et des Systèmes
Massimo Giudici (massimo.giudici@inphyni.cnrs.fr)
Université Côte d'Azur https://orcid.org/0000-0002-7600-4927

Article

Keywords:

Posted Date: July 12th, 2022

DOI: https://doi.org/10.21203/rs.3.rs-1846582/v1

Temporal Localized Turing Patterns in Vertical External-Cavity Surface-Emitting Laser

A. Bartolo,[1] N. Vigne,[2] M. Marconi,[1] G. Beaudoin,[3] K. Pantzas,[3] I. Sagnes,[3] G. Huyet,[4] F. Maucher,[5] S. V. Gurevich,[6] J. Javaloyes,[5] A. Garnache,[2] and M. Giudici[1]

[1] *Université Côte d'Azur, CNRS, Institut de Physique de Nice, 06560 Valbonne, France*
[2] *Institut d'Electronique et des Systèmes, CNRS UMR5214, 34000 Montpellier, France*
[3] *Centre de Nanosciences et de Nanotechnologies, CNRS UMR 9001,*
Université Paris-Saclay, 91120 Palaiseau, France.
[4] *Université Côte d'Azur, CNRS, Institut de Physique de Nice, F-06560 Valbonne, France*
[5] *Departament de Física, Universitat de les Illes Baleares, C/Valldemossa km 7.5, 07122 Mallorca, Spain*
[6] *Institute for Theoretical Physics, University of Münster,*
Wilhelm-Klemm-Str. 9, 48149 Münster, Germany

Localized structures (LS) in lasers have been actively sought for all-optical information processing. So far, two distinct approaches have been developed for achieving LS: one leading to addressable stationary peaks of light in the transverse section of the resonator, the other leading to addressable mode-locked pulses having a fundamental mode spatial profile. Here we show that temporal localized patterns appear in nearly self-imaging Vertical External-Cavity Surface-Emitting Lasers (VECSELs) with an intracavity saturable absorber. The observed patterns consist of a combination of an axial plane-wave with a set of tilted waves having a hexagonal arrangement in the Fourier space. In the time domain these patterns are individually addressable mode-locked pulses having a duration of about ten picoseconds. The theoretical analysis shows that the emergence of these pulsating patterns is a signature of a Turing instability whose critical wave vector depends on spherical aberrations of the optical elements. Our result shows that large aspect-ratio VECSELs offer unique opportunities for studying spatio-temporal phenomena and it paves the way to the generation of spatio-temporal LS.

I. INTRODUCTION

Large aspect-ratio lasers [1, 2] are a platform for studying pattern formation ruled by paradigmatic partial differential equations [3–8]. A variety of dissipative structures have been experimentally reported as the result of self-organization, including phase singularities [9, 10], Turing instabilities [11] and, in bistable laser cavities, Localized Structures (LSs) [12–16]. The latter, in particular, have attracted a lot of attention in the last twenty years for their application to information processing [17]. LSs are beams of light localized in the transverse section of the laser that can be individually switched on and off by a local perturbation [18–20]. Also named Cavity Solitons [21], LSs were observed in broad-area VCSELs coherently driven by an external field [22] and in an external-cavity laser configuration coupled to a saturable absorber [14, 23, 24]. More recently, the concept of LSs has been extended to the time domain: temporal LSs are individually addressable pulses traveling back and forth inside the cavity [25–28]. Temporal LSs have been implemented in VCSELs operated in regimes of passive mode-locking (PML) [29]. It was shown that, if the cavity round-trip τ is longer than the gain recovery τ_g and above a critical modulation depth of the saturable absorber, a variety of mode-locked states with a different number of pulses per round trip coexist with the off solution. In these conditions, mode-locked pulses become localized and they can be individually addressed [29–31].

These results suggest that semiconductor lasers based on vertical-cavity surface-emitting technologies with intracavity saturable absorber may host temporal LSs and, at the same time, fulfill the large aspect-ratio condition. Accordingly, these devices would be a laser platform ideally suited for the experimental observation of spatio-temporal phenomena, a research subject of rising importance [32–36]. In particular, this platform may provide the conditions for the existence of spatio-temporal LSs, also called dissipative Light Bullets [37, 38] , whose experimental observation is still elusive.

Recently it was shown that an optically pumped Vertical External-Cavity Surface-Emitting Laser (VECSEL) with a semiconductor saturable absorber mirror (SESAM) can be properly engineered to emit localized mode-locked pulses [39]. However, the large-aspect ratio condition in VECSEL requires the combination of a nearly self-imaging (SI) external cavity **(author?)** [13, 14, 40] together with a broad area pumped section. These two conditions were not fulfilled in [39], leading to a VECSEL that could only be operated in the single-transverse mode emission.

In this paper we describe the realization of a large-aspect ratio VECSEL and we report on the observation of temporal localized patterns consisting of a combination of an axial plane-wave with a set of tilted waves having a hexagonal arrangement in the Fourier space. These plane waves are nonlinearly coupled and their interference gives birth to an hexagonal pattern in the near-field emission profile. In the time domain these patterns are individually addressable mode-locked pulses having a duration of about ten picoseconds. We show theoretically that the emergence of these pulsating patterns is the signature of a Turing instability whose critical wave vector is determined by spherical aberrations of the optical elements. Our result shows that large aspect-ratio VECSELs are promising laser platforms for investigating a rich variety of spatio-temporal phenomena, including spatio-temporal LS. The theoretical analysis reveals the leading role of spherical aberrations in pattern formation when approaching SI condition, thus suggesting that spatial localization will require aberration engineered optical elements.

II. RESULTS

We consider an L-shaped VECSEL delimited by the gain mirror (also called 1/2 VCSEL) and by a SESAM (see Fig. 1). The output beam is sent to the detection part where the far-field and near-field profiles are imaged on two CCD cameras. The near-field is also imaged on an array of optical fibers for spatially resolved detection at 10 GHz bandwidth. Finally, the total emission is monitored by a 33 GHz bandwidth detection system and by an optical spectrum analyzer. The gain mirror is based on a GaAs substrate with 12 strain-balanced InGaAs/GaAsP quantum wells (QWs) designed for barrier optical pumping and emitting at 1.06 μm. It has been designed for standing the high level of losses in the plane-plane external cavity (see Suppl. Mat. V A). The SESAM features a single strained InGaAs/GaAs QW located near the external surface [42] leading to recombination rate approximately two orders of magnitudes faster than the gain medium. It has been engineered for achieving a modulation depth larger than 8 % between the saturated regime and the unsaturated one (saturable losses) which appears to be critical for obtaining bistability of the VECSEL close to threshold [39]. Moreover, the amount of saturable losses experienced by the electromagnetic field inside the cavity is varied by tuning the gain mirror and the SESAM microcavities resonances (λ_G and λ_{SA} respectively), $\delta\lambda = \lambda_{SA} - \lambda_G$), as detailed in Suppl. Mat. V A The gain mirror is optically pumped at 808 nm by a flat-top elliptical profile having an horizontal axis of 90 μm and a vertical one of 50 μm (see Supp. Mat. V B).

The external cavity has been designed to fulfill the requirement $\tau > \tau_g$ and SI condition after one roundtrip. In addition, the SESAM and gain mirror need to be placed in conjugate planes with a magnification factor larger than one for saturating efficiently the SESAM. In the cold cavity situation, these requirements can be achieved through

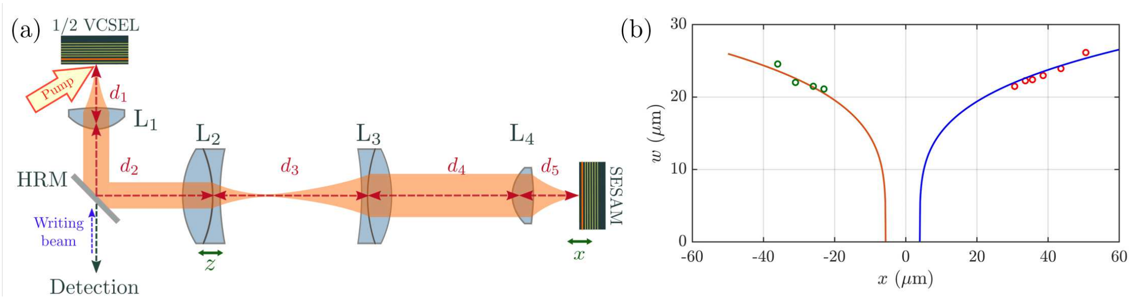

Figure 1. a) Experimental set-up showing the L-shape 8f cavity VECSEL. d_1: distance between the gain section and lens L_1, d_2: distance between L_1 and lens L_2, d_3: distance between L_2 and lens L_3, d_4: distance between $L_3$and lens L_4, d_5: distance between L_4 and the SESAM, HRM= high reflectivity beam splitter (>99.5% at 1.060 nm). b) Waist size of the fundamental Gaussian mode on the gain section calculated with Eq. 7 (Methods IV) as a function of the position of the SESAM ($x = d_5 - f_c$) for f_{th}=40 mm and for two positions of z : z = 2.5 mm (blue curve) and z = −3.5 mm (red curve). For f_{th} = 40 mm, SI condition condition is given by: $z_0 = -0.8\,\text{mm}$, $x_0 = -1.3\,\mu\text{m}$, hence, in terms of $\Delta z = z - z_0$, $\Delta z = +3.3$ mm (blue curve) and $\Delta z = -2.7$ mm (red curve). These numerical curves fit with good agreement the experimentally measured values of the waist obtained when the VECSEL is pumped at 230 mW, which gives rise to a thermal lens with focal length of $f_{th} \approx 40$mm [41]. The position of L_2 has been shifted by +6 mm around its telecentric position from the green circles series of measurements to the red circle ones.

a telecentric arrangement of appropriate optical elements. However, the presence of a pump-induced lens onto the gain mirror modifies sensibly the positions of lenses for achieving SI condition. This spurious lens has a thermal and electronic origin and its focal length f_{th} depends on the pump level [41]. SI condition can be restored only by modifying the position of at least two lenses in the cavity around their telecentric position. Accordingly, we adjust submicrometrically the position of the SESAM ($x = d_5 - f_c$) and of L_2 ($z = d_2 - (f_c + f_2)$). As shown in Methods (and Suppl. Mat. V C), the one-way propagation matrix from the SESAM to the gain mirror can be used to determine SI condition ($z_0(f_{th})$, $x_0(f_{th})$) and to calculate the waist value of the fundamental Gaussian mode w as a function of x and z around SI condition positions. As shown in Fig. 1b), close to SI condition, the waist of the fundamental Gaussian as a function of the position of the SESAM $w(x)$ exhibits an opposite behavior depending on whether $\Delta z > 0$ or $\Delta z < 0$, where $\Delta z = z - z_0$ indicates the misplacement of L_2 with respect to the SI condition. For negative values of Δz (red curve in Fig. 1 b)), w increases when approaching the SESAM to L_4. For $\Delta z > 0$ (blue curve in Fig. 1b)) w increases with the distance between the SESAM and L_4. This behavior is clearly observed in the experiment and it enables an accurate observational assessment of the SI condition.

For finite positive (negative) values of Δz, cavity stability requires $\Delta x > 0$ ($\Delta x < 0$), where $\Delta x = x - x_0$ indicates the misplacement of the SESAM with respect to SI condition (see MethodsIV). As shown in Fig. 1 b), the waist of the fundamental Gaussian decreases as $\mid \Delta x \mid \rightarrow 0$ and, when $\mid w \mid < 20\,\mu$m, spatially extended patterns appear to match the broad pumped section. In Fig. 2 we show the time-averaged spatial profile of a typical pattern observed when $\Delta x \rightarrow 0^+$, for a finite positive value of Δz. This pattern cannot be interpreted as a transverse mode imposed by the boundaries of the resonator, as the ones of Hermite-Gauss or Laguerre-Gauss families. While the latter self-transform in the Fourier space, the pattern shown in Fig. 2 exhibits non homothetic near field and far field profiles. The far field profile reveals a bright central spot surrounded by a nearly hexagonal arrangement of weaker spots at 7° with respect the optical axis of the resonator. The regularity of this arrangement is affected by the presence of inhomogeneities on the gain section and the SESAM used. However, these spots are always equidistant from the bright center spot. In the near field we observe an hexagonal pattern with some bright spots. We have analyzed the relationship between the near field profile and each wave-vector component observed in the far field, as shown in Fig. 2 c-f). If we consider only the axial component (central spot in the far field profile), the corresponding near field profile has a Gaussian shape (Fig. 2 d). This component comprises 90% of the optical power of the pattern. If the central spot in the far-field is filtered out, the near field profile obtained has twice the spatial frequency compared to the one obtained without the filter as can be observed in e). This indicates that the near-field profile is determined by the interference between an on-axis plane wave and the hexagonal set of tilted waves which are phase locked. The pattern shown in Fig. 2 is emitted by the VECSEL within a short range of x, for pumping powers 285 mW$< P_p <$ 400mW and for a detuning range between the microcavities resonances 4.5 nm$< \delta\lambda <$ 8 nm. Within these ranges, the time-averaged profile shown in Fig. 2 is not affected significantly by parameter changes.

The time behavior of the pattern is shown in Fig. 3 a). It features multistability between a set of mode-locked states with a number of pulses per roundtrip ranging from zero to five. The corresponding bifurcation diagram of these pulsating solution versus the pump power P_p is explored in Fig. 3 b). Upon increasing the pumping level (P_p), the off solution loses its stability at P_p = 320 mW at the advantage of a five-pulses per roundtrip mode-lock state.

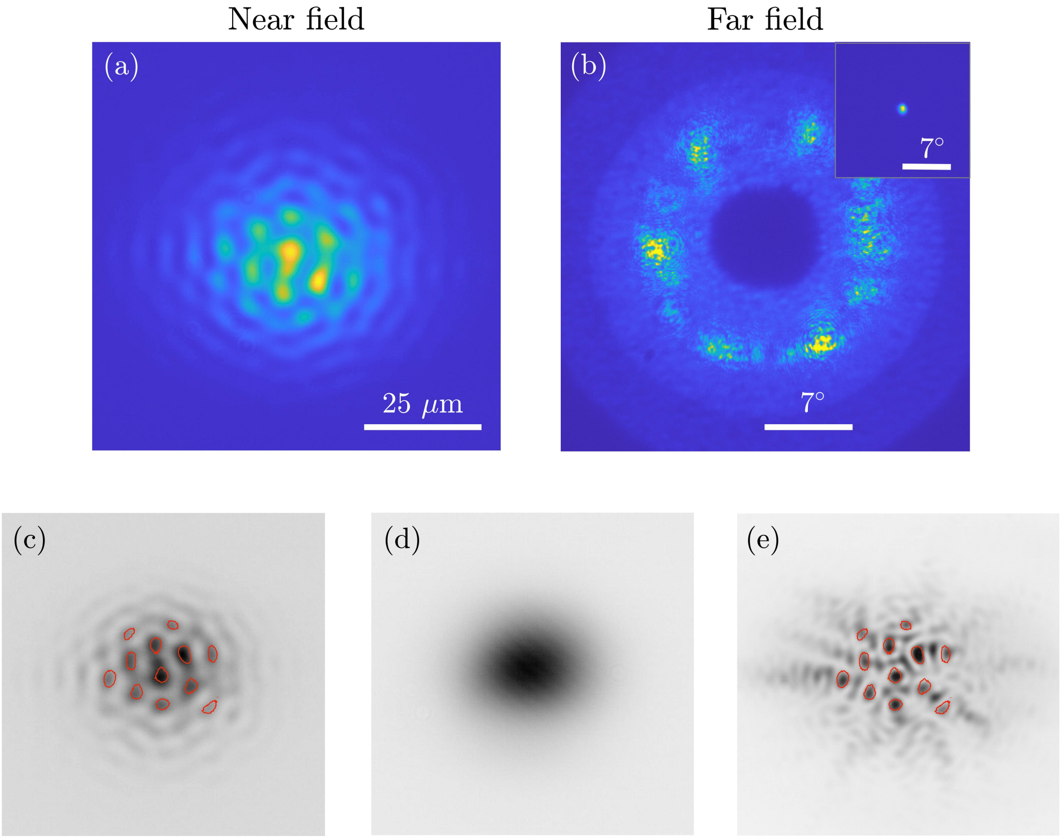

Figure 2. a) Near field and b) Far field time-averaged profiles of the patterns observed when $\Delta z = +3.3$mm and $22\mu\text{m} < x < 27\mu$m. VECSEL is pumped at 320 mW and $\delta\lambda$=5nm. In panel b) the far field has been obtained by filtering out the central part of the profile which carries 90% of the total emitted and hinders the off axis components on the CCD camera. The unfiltered far-field profile is plotted in the inset. This kind of pattern is observed in the range 0.1 mm$< \Delta z <$ 4 mm. As $\mid \Delta z \mid \rightarrow 0$, its existence range in x gets narrower and it requires higher level of pumping. c) Near-field profile with intensity peaks circled in red, d) Near-field profile after filtering out the off-axis Fourier components of the pattern and leaving only the central spot, e) Near-field profile after filtering out the on-axis Fourier components of the pattern (central spot of in the far-field). The contour of the peaks of the total pattern identified in c) are plotted in red.

Then, by decreasing P_p, the VECSEL emission switches to states with a lower number of pulses per roundtrip and, at every jump, P_p is increased to determine the stability of each branch and, when P_p<285 mW, the VECSEL switches to the off solution. The width of the pulse is below the time resolution of our detection system (10 ps, 33 GHz) and auto-correlation measurements of the electromagnetic field gives a coherence time of 2.6 ps which is in agreement with the spectral envelope of 1 nm (267 GHz) FWHM shown Fig. 3 c). Spatially resolved measurements at different points of the pattern reveal that the whole pattern is pulsating as a unique coherent structure.

The multistabilty between different mode-locked states shown in Fig. 3 indicates that the patterns observed are temporal LSs, i.e. they are individually addressable pulses traveling back and forth in the external cavity [29, 43]. In order to demonstrate the possibility of using these pulsating patterns as bits of informations, we have injected a short pump pulse into the gain section to write these temporal localized patterns individually. The system is prepared in the multistable parameter region (285mW$< P_p <$ 318mW) where LSs exist and the amplitude of the addressing pump pulse is chosen to be sufficiently large to bring the system beyond the upper limit of the multistable region, where only the solution composed on five pulses per roundtrip is stable. The addressing pulse is sent to the gain section synchronously with the cavity roundtrip for about one thousand roundtrips. The addressing process is depicted in Fig. 4 by using a space-time diagram where the pump pulse is represented using a color code, while the trajectory of the LS is represented by a black trace. In Fig. 4 we illustrate the writing operation. In Fig. 4 (left), we choose an

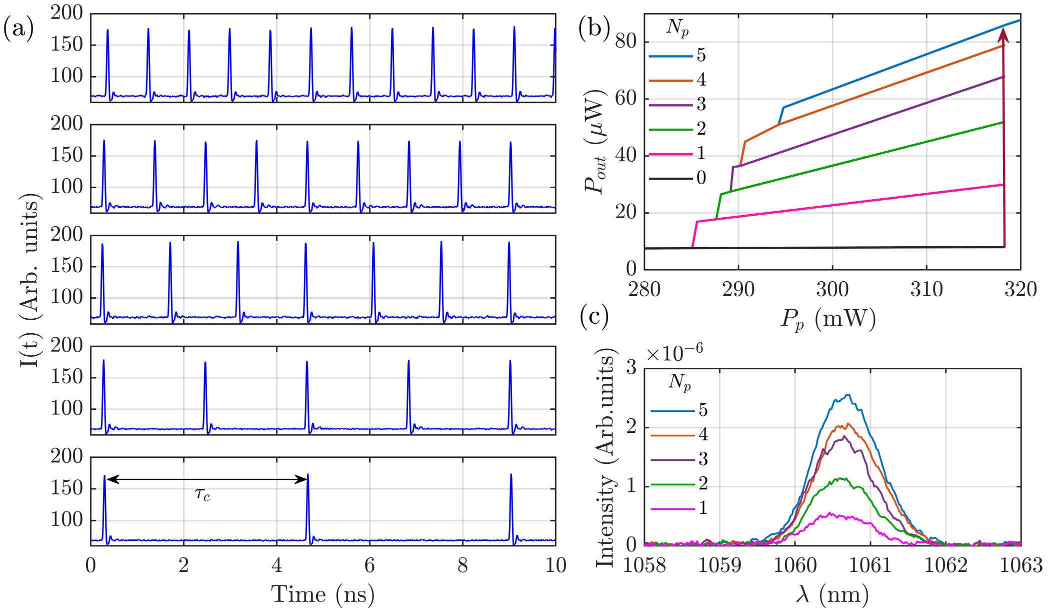

Figure 3. Spatially integrated intensity output of the pattern shown in Fig. 2. a) Coexisting pulsating states of the pattern, b) Total output power emitted by the VECSEL versus the pump power P_p for different pulsating states of the pattern, ranging from no pulse to five pulses per roundtrip, c) Optical spectra corresponding to different pulsating states of the pattern.

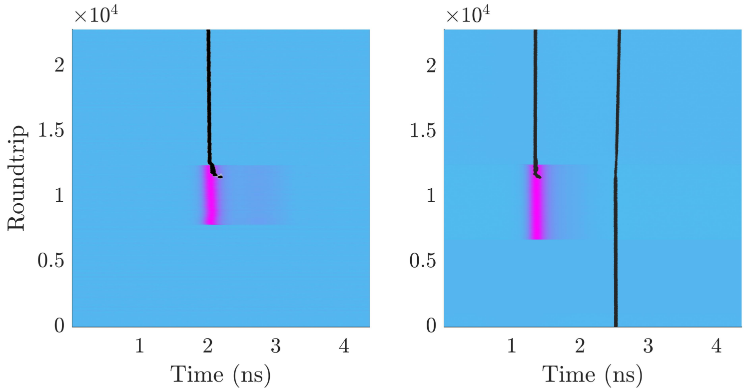

Figure 4. Spatio-temporal diagram of the writing process of a time localized pattern. The trajectory of the LS is represented by a black trace, while the pump evolution is represented on the space time diagram using a color code is by sending a 120 ps pulse to the gain section between (left) round-trip $n_1 = 7800$ and round-trip $n_2 = 12500$ and (right) between round-trip $n_1 = 6800$ and round-trip $n_2 = 12500$. The pulsed pump beam has a Gaussian spatial profile and a waist of 13 μm

initial condition where no LS is present inside the cavity before the addressing pulse. The pump pulse is sufficiently short to switch on a single LS which persists after the perturbation is removed. In Figure 4 (right) we repeat the operation with a LS already existing in the cavity before the dressing pulse. Other initial conditions can be chosen with similar results, provided that the addressing pulse is separated in time from the preexisting LS of at least τ_g.

III. DISCUSSION AND THEORETICAL ANALYSIS

Our experimental results provide evidence of a novel spatio-temporal laser regime which, to the best of our knowledge, can hardly be traced back to any laser model in the literature. Stationary pattern emission from large-aspect ratio laser has been previously observed and explained as a Turing instability leading to transverse traveling waves [10, 11, 44]. The physical origin of this instability has been attributed to the presence of a (positive) detuning between the gain curve resonance and the closest resonator resonance. The laser emits tilted waves whose frequency matches the gain resonance and whose longitudinal wave vector fulfill the resonance condition of the resonator. This mechanism does not apply to our system where the set of longitudinal cavity resonances is very dense (less than 500 MHz free spectral range) compared to the width of all other relevant spectral filtering curves, such as microcavities resonances ($>$ 3.5 nm, i.e. $>$1 THz, see Supp. Mat. V A), gain and saturable absorption curves (more than 10 THz).

In order to describe the spatio-temporal dynamics observed we employ the Haus master equation for PML adapted to the long cavity limit [43, 45]. However, this leads to a four dimensional, stiff, multi-scale partial differential equation (PDE). A qualitative model for the dynamics of the transverse profile of temporal LS, such as the one derived in [37, 46], can be obtained adapting New's method of PML [47] to the situation at hand. This method exploits the scale separation between the pulse evolution, the so-called fast stage in which stimulated emission is dominant, and the slow stage that is controlled by the gain recovery processes. Under the hypothesis that the spatio-temporal profile can be factored into a product of a transverse profile and a short temporal pulse that corresponds to the temporal LS, one can obtain a simplified description of the slow evolution of the transverse profile of the temporal LS $A\left(r_\perp,\theta\right)$ as

$$\frac{\partial A}{\partial \theta} = \left[f\left(|A|^2\right) + \mathcal{L}_\perp\right] A, \tag{1}$$

where θ is the round-trip number and we defined the effective nonlinearity as

$$f\left(P\right) = \left(1 - i\alpha_1\right) J_1\left(r_\perp\right) h\left(P\right) + \left(1 - i\alpha_2\right) J_2 h\left(sP\right) - k, \tag{2}$$

The nonlinear response of the active material to a pulse is $h\left(p\right) = \left(1 - e^{-p}\right)/p$. We define k as the round-trip cavity loss and in Eq. (2) we introduced the line-width enhancement factors α_j of the two active media, that relax toward the pumping power J_j. The ratio of the saturation fluences of the absorber and of the gain is denoted by the parameter s. The effect of finite size optical pumping is taken into account by the spatial dependence of $J_1\left(r_\perp\right) > 0$. Saturable absorption is obtained by setting $J_2 < 0$. It is worth noting that, if the function $h(P)$ is replaced by the Lorentzian line saturation for continuous wave beams $h\left(P\right) \to 1/\left(1+P\right)$ in Eqs. (1,2), one obtains the equations obtained in [48, 49], used for describing (stationary) spatial auto-solitons in continuous wave bistable interferometers.

The spatio-temporal linear operator $\mathcal{L}_\perp$ can be determined by using the Fresnel transform [50], which permits the analytical calculation of the transverse effects occurring at each round-trip from the round-trip ABCD matrix. The latter includes diffraction and wavefront curvature occurring in the quasi-telecentric cavity as well as diffraction and thermal lensing (in the parabolic approximation) taking place within the microcavities. In addition, we considered the influence of weak spherical aberrations. The latter are essentially due to the presence of the two short focal distances collimators L_1 and L_4 which are challenged by wide angular spread of the beams. In agreement with experimental observations we assume that $f_c\left(r_\perp\right) = f_0 + \sigma r_\perp^2$ with $\sigma \ll 1$ representing a small aberration coefficient. For the experimental conditions (nearly SI condition and $f_0/f_{2,3} \ll 1$), the effect of spherical aberration can be analytically reduced to a transverse Bilaplacian operator. The details of these calculations will be discussed elsewhere. Describing the wavefront curvature, the diffraction and aberrations as small perturbations to the field profile at each roundtrip, the spatio-temporal linear operator $\mathcal{L}_\perp$ reads

$$\mathcal{L}_\perp = i\widetilde{C}r_\perp^2 + \left(d + i\widetilde{B}\right)\nabla_\perp^2 + i\widetilde{S}\nabla_\perp^4\,, \tag{3}$$

where we define the following dimensionless parameters: the effective diffraction parameter $\tilde{B} = \lambda B_{RT}/\left(4\pi\right) + l_{1,\perp}^2 + l_{2,\perp}^2$, the wavefront curvature $\tilde{C} = \pi C_{RT}/\lambda$ and the aberration parameter $\tilde{S} = \left(\frac{\lambda}{2\pi}\right)^3 \sigma f_0^2$. Here, B_{RT} and C_{RT} are, respectively, the coefficients of the ABCD roundtrip matrix defined in IV and $l_{j,\perp}$ being the normalized micro-cavity diffraction lengths. As shown in IV, close to self-imaging conditions, $B_{RT} \approx 2(M^2\Delta x)$ and $C_{RT} \approx -2\frac{\Delta z}{f_c^2}$, hence Δx controls the diffraction while Δz rules the wavefront curvature which is equivalent to a parabolic transverse potential in Eq. 3. The finite size of lenses and the numerical aperture of the whole optical system is modeled by a diffusion parameter d that penalizes high transverse spatial frequencies $q_\perp$.

Close to SI condition, for positive diffraction ($\Delta x \gtrapprox 0$), the VECSEL resonator is stable for focusing wavefront curvature ($\widetilde{C} \lessapprox 0$, i.e. $\Delta z \gtrapprox 0$). Experimental results show that, when $\widetilde{B} \to 0$, a modulated pattern featuring well defined transverse wave vectors appear. This phenomenology can be explained as the result of a supercritical Turing instability. It was shown in [51] that Eq. (1) forbids the appearance of a Turing instability while it allows for a long wavelength instability and the formation of a band of unstable spatial frequencies in the range $q \in [0, q_M]$. However, the presence of the Bilaplacian operator describing optical aberrations changes this picture, as it introduces a new spatial scale in the system and it renders the appearance of a Turing bifurcation possible. This is shown in Fig. 5(a) where we plot the result of the stability analysis of the homogeneous state for a value of the pump within the bistability region where the VECSEL emits temporal LS. The real part of the two dominant eigenvalues reveals the presence of a Turing instability at a wave-vector $q_T \simeq \sqrt{\widetilde{B}/\widetilde{S}}$ in addition to the band of unstable spatial frequencies in the range $q \in [0, q_M]$. It is worth noting that the finite size of the pump profile imposes a low frequency cut-off for the

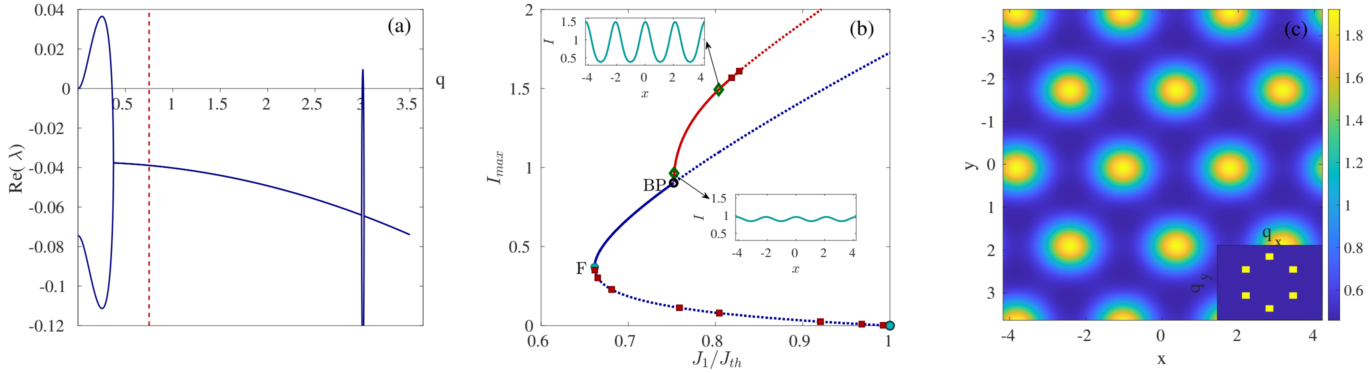

Figure 5. (a) Stability analysis of the uniform solution over the upper state of the bistable solution branch. A long wavelength modulational instability band is present, however it is inhibited for a system size of $L_\perp = 8.3776$ which corresponds to a low frequency cut-off of $q_c = 2\pi/L_\perp = 0.75$ (orange vertical dashed line). A second narrow band that corresponds to a Turing instability may appear at a wavevector $q_T \simeq \sqrt{\widetilde{B}/\widetilde{S}} = 3.01$. This diagram is obtained after the emergence of the Turing instability for a value of $J_1 = 0.78 J_{th}$ that corresponds to an intensity $I = 1$. It is above the fold located at $J_F \simeq 0.661 J_{th}$. (b) A branch of CW (blue) and spatially periodic (red) solutions of Eq. 1. The intensity of the field is shown as a function of the scaled gain bias J_1/J_{th}. The stable (unstable) solutions are depicted as solid (dashed) lines. The unstable CW branch bifurcates unstable from the off state and it is stabilized at the fold **F**. The stable periodic branch that corresponds to rolls bifurcates from the CW solution at the branching point BP (black circle) which corresponds to a Turing bifurcation. The emerging pattern further losses its stability via an Andronov-Hopf bifurcation (red square). The two insets show the intensity of the emerging periodic pattern at the points marked as green diamonds. (c) Equivalent regime in two dimensions where we show the intensity profile as well as the far field Fourier spectrum after removal of the on axis homogeneous component (inset). It consists in a regular hexagonal pattern whose wave-vector is $|q_T| \simeq 3$ is given by the stability analysis of the uniform state. The bias current is $J_1 = 0.777 J_{th}$ and $(L_x, L_y) = (8.378, 7.255)$. Other common parameters are: $\widetilde{B} = 1, \widetilde{C} = 0, S = 0.11, \alpha_1 = 1.5$, $\alpha_2 = 0.5$, $J_2 = -0.12$, $k = 0.1$, $s = 15$, $d = 0.003$,

wave-vectors allowed in the system, $q_c = 2\pi/L_\perp$. This spatial frequency filtering eventually controls which instability can develop : if $q_M < q_c$ the long wavelength instability is inhibited and the Turing pattern remains the unique spatial instability that can emerge, provided that q_T is resonant, i.e. an integer multiple of q_c, i.e with $n \in \mathbb{N}$. Consequently, this instability can be expected to appear by tuning the value of $\widetilde{B}$ within narrow range, in good agreement with experimental observations.

In Fig. 5(b) we show the result of numerical simulations of Eq. (1) as well as path continuation using Pde2Path [52] for a system with one transverse spatial dimension and with homogeneous pumping. It reveals that a homogeneous emission of temporal LS appear subcritically below the lasing threshold. The corresponding C-shape is represented by the blue line in Fig. 5(b). When the system size is chosen such that $q_T/q_c = 4$, a periodic pattern can emerge from a homogeneous emission while increasing the pump power. As in the experiment, the periodic pattern appears as a modulation of an homogeneous on-axis emission which dominates the far-field profile. This Turing pattern can be observed at a fixed pump level by tuning the value $\widetilde{B}$, as this parameter will change the value of the critical wave-vector q_T with respect to $4q_c$. In this case the pattern will appear with a finite modulation amplitude of the homogeneous emission, fixed by the pump power. In two transverse dimensions, the dynamics is more complex since only the magnitude of the unstable wave-vector $|q_T|$ is fixed by the linear stability analysis leading to an annular distribution of unstable wave vectors in the two-dimensional plane spanned by $q_\perp = (q_x, q_y)$. Stripes, squares or hexagonal patterns can be selected depending on the kind of nonlinearity coupling the different wave-vectors that must all emerge with magnitude $|q_T|$. However, the structure of the nonlinearity in Eq. 1 favors the emergence of hexagonal patterns as can be seen in Fig. 5(c). The far field represented in the inset of Fig. 5(c) exhibits (in Log scale) the typical spectrum associated with hexagonal patterns after filtering out the on-axis component. The value of $q_T \sim 3$ matches the result of the linear stability analysis.

In conclusion, we have realized and operated a laser platform enabling the investigation of fully developed spatio-temporal dynamics. In this paper, we have reported the first observation of temporal localized Turing patterns, but other novel laser regimes will be investigated in the future. In particular, the spatial shaping of the pumped region opens interesting perspectives since, thanks to SI condition, the near-field emission profile of the laser will be governed by the pump profile. Preliminary results indicate the possibility of obtaining spatially decorrelated spots in the transverse plane emitting temporal LS. In addition, the near-field emission profile can be shaped arbitrarily, reproducing, for example, alphabetic letters and geometrical figures. In terms of applications, this platform can be used for the spatio-temporal processing of information, for implementing multiple sources of reconfigurable frequency combs sharing the same active media [53], as well as for speckle-free imaging with short pulses [54].

IV. METHODS

External cavity design. The VECSEL external cavity (see Fig. 1a)) has been designed to fulfill the requirement $\tau > \tau_g$ for temporal localization, which means, with $\tau_g \sim 1$ns, a cavity length larger than 500 mm ($\tau > 3$ ns). In order to reach this length we used a four-lenses arrangement where the first lens (L1, the one closest to the gain section) and the last lens (L4, the one closest to the SESAM) are large numerical aperture aspheric collimators ($f_1 = f_4 = f_c =$8 mm) and L2 and L3 are achromatic lenses having $f_2 = 100$mm and $f_3 =$200 mm. The resonator is L-shape delimited by the gain mirror (also called 1/2 VCSEL) and by a SESAM. Light extraction occurs by transmission through a high reflective beam splitter (>99.5 reflectivity at 1.060 nm) which reflects the intracavity radiation beam. This geometry avoids anisotropies that would have been introduced by using a linear cavity with a beam splitter transmitting the intracavity radiation beam. The lenses are placed in a telecentric arrangement (8f), i.e. the distances between the lenses are given by the sum of their focal lengths (d_1=f_1, d_2=f_1+f_2, d_3=f_2+f_3, d_4=f_3+f_4, d_5=f_4), thus making a total cavity length L=632 mm (cavity round-trip time $\tau \approx 4.2$ ns). This arrangement ensures, at least in the cold cavity situation, that the gain section and the SESAM are in conjugate planes and that SI condition is met.

Temporal LS (and mode-locking in general) relies on the possibility of saturating effectively the SESAM at fluence levels well below the saturation fluence of the gain section (F_G) . Even if these elements are designed such that $s = F_G/F_B$=6, being F_B the saturation fluence of the SESAM, an effective method for increasing s is to introduce a magnification factor M of the SESAM near-field image onto the gain section. In the telecentric arrangement described above $M = f_3/f_2$ and we choose $f_2 = 100$mm and $f_3 =$200 mm to have $M = 2$.

In terms of ABCD transfer matrix from the gain section to the SESAM , the telecentric arrangement gives $\begin{pmatrix} x' \\ \theta' \end{pmatrix} = \begin{pmatrix} 1/M & 0 \\ 0 & M \end{pmatrix} \begin{pmatrix} x \\ \theta \end{pmatrix}$, which describes an imaging condition with demagnification between the two elements and SI condition after a roundtrip. However, the presence of a pump induced lens onto the gain section modifies sensibly the positions of lenses for achieving SI condition with respect to the cold cavity situation. This pump induced lens has a focal length f_{th} spanning from 10 to 80 mm depending on the pump level [41] (Supp. Mat. V B) Self-imaging condition in presence of this spurious lens can be obtained only by modifying the position of at least two lenses in the cavity around their telecentric position. The most effective choice, considering also practical experimental considerations, is to adjust micrometrically of the position of the SESAM and the position of L_2. By calling x the offset of d_5 with respect to telecentric position ($x = d_5 - f_c$) and z the offset of d_2 with respect to telecentric position ($z = d_2 - (f_c + f_2)$), the one way propagation matrix from the gain section to the SESAM then reads (see Suppl. Math. C for full calculations):

$$\begin{pmatrix} A & B \\ C & D \end{pmatrix} = \begin{pmatrix} 1/M + (\frac{f_c^2 z}{M f_2^2} - Mx)(\frac{1}{2f_{th}} + \frac{z}{f_c^2}) & Mx - \frac{f_c^2 z}{f_2^2 M} \\ M(-\frac{1}{2f_{th}} - \frac{z}{f_c^2}) & M \end{pmatrix} \tag{4}$$

For a given value of f_{th}, $C = 0$ (and $A = 1/M$) for $z = z_0 = -\frac{f_c^2}{2f_{th}}$, while $B = 0$ for $x = x_0 = -\frac{f_c^4}{2M^2 f_2^2 f_{th}}$. For $f_c =$ 8 mm and typical values of f_{th} one finds that z_0 is of the order of few millimeters, while x_0 will be of few microns since $f_2 >> f_c$. Hence, by adjusting z and x it is possible to achieve SI condition for any value of f_{th}.

From the experimental point of view, the precision requirement on the positions of the optical elements make unrealistic to achieve SI condition by placing these elements at the calculated positions. We describe the deviations from SI condition by introducing $\Delta x = x - x_0$ and $\Delta z = z - z_0$. Then, we can rewrite Eq. 4:

$$\begin{pmatrix} A & B \\ C & D \end{pmatrix} = \begin{pmatrix} 1/M + \frac{(\Delta z)^2}{M^2 f_2^2} - \frac{\Delta x \Delta z}{f_c^2} & M\Delta x - \frac{f_c^2 \Delta z}{f_2^2 M} \\ -M\frac{\Delta z}{f_c^2} & M \end{pmatrix} \tag{5}$$

The round-trip matrix reads

$$\begin{pmatrix} A_{RT} & B_{RT} \\ C_{RT} & D_{RT} \end{pmatrix} = \begin{pmatrix} 1 + 2BC & 2DB \\ 2AC & 1 + 2BC \end{pmatrix} \tag{6}$$

Accordingly, the waist of the fundamental Gaussian beam on the gain section in mm is given by

$$w = \sqrt{\frac{(1.06 \cdot 10^{-3}/\pi)|2DB|}{\sqrt{1-m^2}}} \tag{7}$$

where $m = 1 + 2BC$ is half the trace of the roundtrip matrix. For cavity stability $-1 < m < 1$, which implies $-1 < BC < 0$. As shown in Suppl. Math. C, for small deviation of z from the SI condition, the stability of the cavity requires $\Delta x > 0$ when $\Delta z > 0$ and $\Delta x < 0$ when $\Delta z < 0$. The analysis of Eq. 7 shown in Fig. 1 b) provides an observational protocol for assessing SI condition as the positions of L_2 and of the SESAM are varied. Finally, it is worth noting that, close to SI condition, the ABCD roundtrip matrix can be approximated to

$$\begin{pmatrix} A_{RT} & B_{RT} \\ C_{RT} & D_{RT} \end{pmatrix} = \begin{pmatrix} 1 & 2(M^2\Delta x) \\ -2\frac{\Delta z}{f_c^2} & 1 \end{pmatrix} \tag{8}$$

V. SUPPLEMENTARY MATERIALS

A. VECSEL description

The VECSEL realized in this paper have been designed for studying fully developed spatio-temporal dynamics in a laser platform. More specifically, the goal is to gathering within the same laser the requirements for hosting spatial and temporal localized structures (LS). While the former require a large aspect-ratio laser with a broad-area pumped region and self-imaging external cavity, the former requires an external cavity roundtrip larger than the gain recombination time. Both regimes require a bistable response which can be provided by an intracavity saturable absorber (semiconductor saturable absorber mirror, SESAM). For temporal localization, previous experimental results and numerical simulations, indicate that modulation depth of the SESAM is a crucial parameter for achieving temporal localization [29, 39, 55]. Finally, spatial homogeneity of the VECSELs samples is required for studying spatial LS formation and properties [56].

Optically-pumped VECSELs based on mature GaAs growth technologies for emission wavelength at 1.06 μm appear to be the most promising devices for fulfilling the spatial homogeneity and broad-area pumping requirements described above. In addition, the SESAM has been processed at high temperature for ensuring the best spatial homogeneity (less than 10000 defects per cm^2). Concerning VECSEL operation in a nearly SI external cavity, it is important to point out that VECSELs cavities are usually designed for confining transversely the electromagnetic field according to a Gauss-Laguerre basis and for favoring lasing emission onto the fundamental Gaussian mode. In our platform this guiding mechanism is lacking and the VECSEL needs to rely onto a gain section capable of standing a high level of losses in the external resonator.

Accordingly, we realize a gain mirror with 12 strain-balanced InGaAs/GaAsP quantum wells (QWs) and a confinement factor enhanced to $\Gamma = 4.5$ by adding 2 Bragg pairs on the top of the gain mirror. This leads to a micro cavity bandwidth of $\Delta\lambda_G = 9\,\mathrm{nm}$ (FWHM) of the gain mirror, to a saturation fluence above $F_G = 25\,\mu\mathrm{J/cm}^2$and a gain level at maximum pumping of 20 %. Carrier lifetime is around $\tau_g = 1 - 2\,\mathrm{ns}$ depending to the pump level. To keep the external-cavity losses at the lowest level, the reflectivity of the gain mirror has been maximized (>99,9%) and the unsaturable losses of the SESAM have been minimized to less than 0.3 %.

While the experimental results described in this paper have been obtained by using the above described gain mirror, similar results have been obtained with another sample having 6 strain-balanced InGaAs/GaAsP QWs and a confinement factor enhanced to $\Gamma = 12$ by adding 3 Bragg pairs on the top of the gain mirror. This leads to a micro cavity bandwidth of $\Delta\lambda_G = 3.5\,\mathrm{nm}$ (FWHM) of the gain mirror, to a saturation fluence above $F_G = 10\,\mu\mathrm{J/cm}^2$and a gain level at maximum pumping of 25 %.

The SESAM structure features a single strained InGaAs/GaAs QW located at $1 \sim 2$ nm from the external surface [42], which enables reaching a fast recombination rate (50 ps) together with high crystal homogeneity. Hence, recombination rate in SESAM is two orders of magnitude faster than in the gain section which is compatible with a stable passive mode-locking and with the existence of temporal LS [55]. SESAM modulation depth of the saturated/unsaturated reflectivity (also called saturable losses) is one of the most critical parameter for the existence of temporal LS [29, 37, 55]. Bistable response of the VECSEL appears for a modulation depth larger than a critical amount. On the other hand, when the unsaturated reflectivity is too high, the VECSEL may not have enough gain to reach the threshold.

The modulation depth of the SESAM has been enhanced by increasing the finesse of the SESAM microcavity defined by the back mirror and the air/semiconductor interface. A top dielectric Bragg mirror formed by a pair of Si/SiN

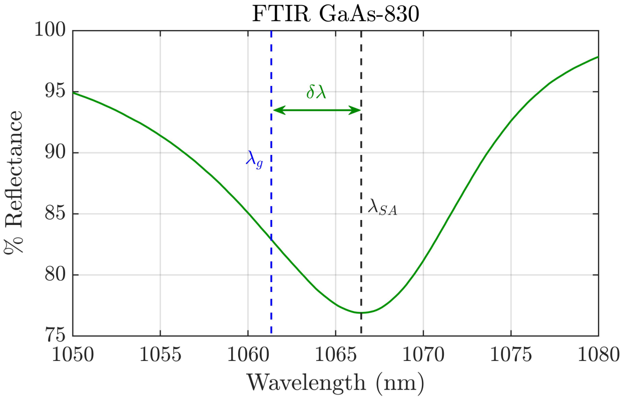

Figure 6. Unsaturated reflectance of the SESAM around microcavity resonance @25°C

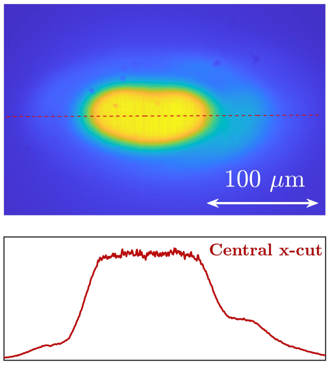

Figure 7. Pump profile onto the gain mirror

layers has been added on this interface, thus leading to a modulation depth of the reflectivity at the micro-cavity resonance peak (1.0667 μm) of $A = 23\%$, a wavelength bandwidth of $\Delta\lambda_B = 15\,\text{nm}$ (FWHM) and saturation fluence $F_B = 4 \sim \mu J/cm^2$. The unsaturated reflectivity of the SESAM is shown in Fig. 6.

Because the gain section microcavity bandwidth is much narrower than the one of the SESAM, the amount of saturable losses experienced by the field in the VECSEL can be varied by changing the detuning $\delta\lambda$ between the gain microcavity resonance and the SESAM one (λ_G and λ_{SA} respectively) , $\delta\lambda = \lambda_{SA} - \lambda_G$. The position of each resonance can be set experimentally through the temperature control of the samples. In Fig. 6 we indicate the smallest value of $\delta\lambda$ for the 12 strain-balanced QWs gain mirror below which the unsaturated losses are too high for the VECSEL to reach threshold.

B. Optical Pump and induced lensing effects

The gain mirror is optically pumped at 808 nm by a single transverse mode diode laser. The Gaussian pump profile is transformed by using a beam shaper to a flat top circular profile having a diameter of 50 μm diameter (see Fig. 7). A flat top pump profile provide a broad-area homogeneously pump region, thus maximizing the aspect-ratio of the VECSEL. Moreover it reduces the thermal-electronics lens effect induced by the pump profile. The pump beam is incident onto the gain mirror device with an angle close to the Brewster angle, thus pumping an elliptical region having an horizontal axis of 90 μm and a vertical one of 50 μm. The maximum pump power reaching the gain section is $P_{p,max} = 500$ mW. The polarization axis is chosen to be in the incidence plane (TM) in order to maximize the light transmitted inside the semiconductor.

The pump profile induces a thermal profile and an electronic profile on the gain section. While the former is equivalent to a converging lens (thermal lens) the latter induces a diverging lens (electronic lens). The thermal lens focal length (f_{th}) depends on the gain section structure, its thermal load and the pump power [41]. In the sample

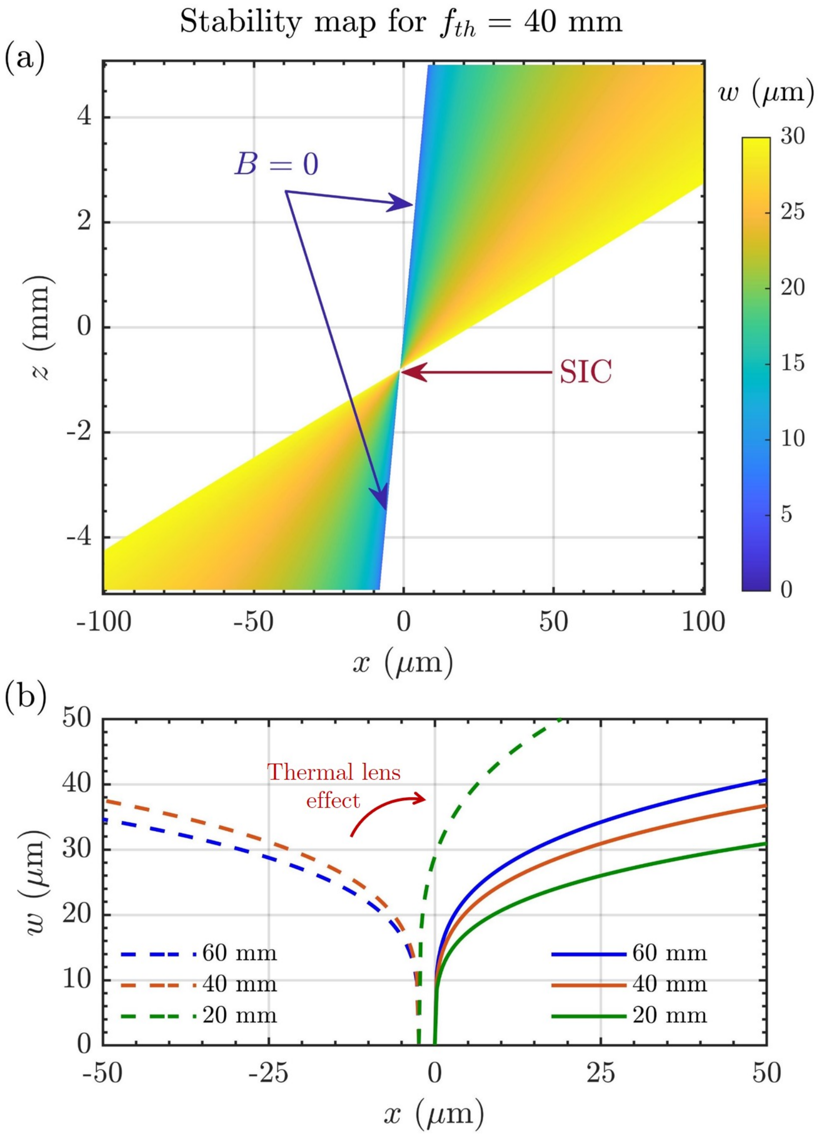

Figure 8. a) Waist of the fundamental Gaussian beam on the gain section as a function of x and z for f_{th}=40 mm. SI condition is located in $z_0 = -0.8\,mm$, $x_0 = -1.3\,\mu m$ b) Waist of the fundamental Gaussian beam on the gain section as a function of x for two values of z : $z = -1.5$ mm (dashed lines) and $z = 0$ mm (continuous line) and for different thermal lenses focal lengths : f_{th}=20 mm (green), f_{th}= 40 mm (orange) and f_{th}=60 mm (blue). While SI condition condition for x (x =x_0) is not changing significantly with f_{th}, for z it does: $z_0(f_{th} = 20\,mm) = -1.6$ mm, $z_0(f_{th} = 40\,mm) = -0.8$mm, $z_0(f_{th} = 60\,mm) = -0.53$ mm. The values of Δz change accordingly: $\Delta z = +0.1$ mm (green dashed line), $\Delta z = +1.6$ mm (green continuous line), $\Delta z = -0.7$ mm (orange dashed line), $\Delta z = +0.8$ mm (orange continuous line), $\Delta z = -0.97$ mm (blue dashed line), $\Delta z = +0.53$ mm (blue continuous line).

used in this paper $f_{th} \approx \frac{10\,mm\,W}{P_p}$, hence it ranges between 70 mm ($P_p = 150$ mW) and 19 mm ($P_p = 500$ mW).

C. ABCD matrix calculation

We write the ABCD transfer matrix from the gain section to the SESAM in presence of a pump induced lens. We refer to distances and focal lengths defined in Fig. 1, the optical elements are placed close to telecentric arrangement (d_1=f_c, d_2=f_c+f_2, d_3=f_2+f_3, d_4=f_3+f_c, d_5=f_c). We introduce two degrees of freedom: x is the offset of d_5 with respect to telecentric position $x = d_5 - f_c$ and z the offset of d_2 with respect to telecentric position $z = d_2 - (f_c + f_2)$. Magnification is given by the ratio between focal lenghts of L_3 and L_2 : $M = f_3/f_2$.

$$\begin{pmatrix} A & B \\ C & D \end{pmatrix} = \begin{pmatrix} 1 & f_c + x \\ 0 & 1 \end{pmatrix} \times \begin{pmatrix} 1 & 0 \\ -1/f_c & 1 \end{pmatrix} \times \begin{pmatrix} 1 & f_c + Mf_2 \\ 0 & 1 \end{pmatrix} \times \begin{pmatrix} 1 & 0 \\ -1/(Mf_2) & 1 \end{pmatrix} \times \begin{pmatrix} 1 & f_2 + Mf_2 - z \\ 0 & 1 \end{pmatrix} \times$$

$$\times \begin{pmatrix} 1 & 0 \\ -1/f_2 & 1 \end{pmatrix} \times \begin{pmatrix} 1 & f_2 + f_c + z \\ 0 & 1 \end{pmatrix} \times \begin{pmatrix} 1 & 0 \\ -1/f_c & 1 \end{pmatrix} \times \begin{pmatrix} 1 & f_c \\ 0 & 1 \end{pmatrix} \times \begin{pmatrix} 1 & 0 \\ -1/2f_{th} & 1 \end{pmatrix} =$$

$$= \begin{pmatrix} 1/M + (\frac{f_c^2 z}{Mf_2^2} - Mx)(\frac{1}{2f_{th}} + \frac{z}{f_c^2}) & Mx - \frac{f_c^2 z}{f_2^2 M} \\ -M(\frac{1}{2f_{th}} + \frac{z}{f_c^2}) & M \end{pmatrix}$$

It is worth noting that, if $z = 0$, the C term of this transfer matrix is always different from zero. Therefore, in presence of a thermal lens, in addition to the position of the SESAM, it is necessary to tune the position of another lens for having the gain section and the SESAM in conjugate planes.

For a given value of f_{th} the condition for having $C = 0$ (and $A = 1/M$) is that $z = z_0 = -\frac{f_c^2}{2f_{th}}$, while $B = 0$ for $x = x_0 = -\frac{f_c^4}{2M^2 f_2^2 f_{th}}$. For $f_c = 8$ mm and typical values of f_{th} one finds that z_0 is of the order of few millimeters for strong thermal lensing, while $x_0$will be of few microns since $f_2 >> f_c$. Hence, by adjusting z and x it is possible to achieve SI condition for any value of f_{th}. By introducing deviation from SI condition for $d_5$and d_2 : $\Delta x = x - x_0$ and $\Delta z = z - z_0$, we can rewrite the transfer matrix:

$$\begin{pmatrix} A & B \\ C & D \end{pmatrix} = \begin{pmatrix} 1/M + \frac{(\Delta z)^2}{M^2 f_2^2} - \frac{\Delta x \Delta z}{f_c^2} & M\Delta x - \frac{f_c^2 \Delta z}{f_2^2 M} \\ -M\frac{\Delta z}{f_c^2} & M \end{pmatrix}$$

The propagation matrix from the SESAM to the gain section is given by$\begin{pmatrix} D & B \\ C & A \end{pmatrix}$ where A,B,C,D are the coefficients of the transfer matrix from the gain section to the SESAM. Hence, the round-trip matrix reads $\begin{pmatrix} 1 + 2BC & 2DB \\ 2AC & 1 + 2BC \end{pmatrix}$, the roundtrip matrix reads:

$$\begin{pmatrix} A_{RT} & B_{RT} \\ C_{RT} & D_{RT} \end{pmatrix} = \begin{pmatrix} 1 - 2\left[M^2 \frac{(\Delta z)(\Delta x)}{f_c^2} - \frac{(\Delta z)^2}{f_2^2}\right] & 2(M^2 \Delta x - \frac{f_c^2 \Delta z}{f_2^2}) \\ -2\frac{\Delta z}{f_c^2}\left[1 + \frac{(\Delta z)^2}{Mf_2^2} - \frac{(\Delta z \Delta x)}{f_c^2}\right] & 1 - 2\left[M^2 \frac{(\Delta z)(\Delta x)}{f_c^2} - \frac{(\Delta z)^2}{f_2^2}\right] \end{pmatrix}$$

The waist of the fundamental Gaussian beam on the gain section in mm is given by

$$w = \sqrt{\frac{(1.06 \cdot 10^{-3}/\pi)|2DB|}{\sqrt{1 - m^2}}} \tag{9}$$

where $m = 1 + 2BC$ is half the trace of the roundtrip matrix. For cavity stability $-1 < m < 1$, which implies $-1 < BC < 0$, i.e. $-1 < -M^2\frac{\Delta x \Delta z}{f_c^2} + \frac{(\Delta z)^2}{f_2^2} < 0$. Close to SI condition, the term in $(\Delta z)^2/f_2^2$ can be neglected and the stability of the cavity requires $\Delta x > 0$ when $\Delta z > 0$ and $\Delta x < 0$ when $\Delta z < 0$. It is worth noting that, close to SI condition, the ABCD roundtrip matrix can be approximated to

$$\begin{pmatrix} A_{RT} & B_{RT} \\ C_{RT} & D_{RT} \end{pmatrix} = \begin{pmatrix} 1 & 2(M^2 \Delta x) \\ -2\frac{\Delta z}{f_c^2} & 1 \end{pmatrix}.$$

In Fig. 8a) we plot $w(x, z)$ in color scale for a given value of f_{th}. In Fig. 8b) we plot the waist of the fundamental Gaussian as a function of x for different values of f_{th} and for two different values of z. By increasing the optical pump intensity, f_{th} decreases, z_0 decreases thus leading to an increase of Δz. Hence, increasing the pump will flatten the curve $w(x, z)$ towards the positive direction of x axis. If Δz is negative for a given pump value it may become positive when increasing pumping, leading to an inversion of the stability of the Gaussian mode from negative to positive values of x (see the green dashed curve in Fig. 8b)).

ACKNOWLEDGMENTS

The INPHYNI Group acknowledges project ANR-18-CE24-0002 BLASON and funding of Région PACA OPTIMAL. J.J. acknowledges financial support from project MOVELIGHT (PGC2018-099637-B-100 AEI/FEDER UE).

---

[1] F.Tito Arecchi, Stefano Boccaletti, and PierLuigi Ramazza. Pattern formation and competition in nonlinear optics. *Physics Reports*, 318(1):1–83, 1999.

[2] L.A. Lugiato. Transverse nonlinear optics: Introduction and review. *Chaos, Solitons and Fractals*, 4(8):1251–1258, 1994. Special Issue: Nonlinear Optical Structures, Patterns, Chaos.

[3] P. Coullet, L. Gil, and F. Rocca. Optical vortices. *Optics Communications*, 73(5):403–408, 1989.

[4] Gian-Luca Oppo, Giampaolo D'Alessandro, and William J. Firth. Spatiotemporal instabilities of lasers in models reduced via center manifold techniques. *Phys. Rev. A*, 44:4712–4720, Oct 1991.

[5] K. Staliunas. Laser ginzburg-landau equation and laser hydrodynamics. *Phys. Rev. A*, 48:1573–1581, Aug 1993.

[6] G. Huyet, M. C. Martinoni, J. R. Tredicce, and S. Rica. Spatiotemporal dynamics of lasers with a large fresnel number. *Phys. Rev. Lett.*, 75:4027–4030, Nov 1995.

[7] J. Lega, J.V. Moloney, and A.C. Newell. Swift-hohenberg equation for lasers. *Phys. Rev. Lett.*, 73:2978–2981, 1994.

[8] P. K. Jakobsen, J. Lega, Q. Feng, M. Staley, J. V. Moloney, and A. C. Newell. Nonlinear transverse modes of large-aspect-ratio homogeneously broadened lasers: I. analysis and numerical simulation. *Phys. Rev. A*, 49:4189–4200, May 1994.

[9] F. T. Arecchi, G. Giacomelli, P. L. Ramazza, and S. Residori. Vortices and defect statistics in two-dimensional optical chaos. *Phys. Rev. Lett.*, 67:3749–3752, Dec 1991.

[10] K. Staliunas, G. Slekys, and C. O. Weiss. Nonlinear pattern formation in active optical systems: Shocks, domains of tilted waves, and cross-roll patterns. *Phys. Rev. Lett.*, 79:2658–2661, Oct 1997.

[11] S. P. Hegarty, G. Huyet, J. G. McInerney, and K. D. Choquette. Pattern formation in the transverse section of a laser with a large fresnel number. *Phys. Rev. Lett.*, 82:1434–1437, Feb 1999.

[12] V. B. Taranenko, K. Staliunas, and C. O. Weiss. Spatial soliton laser: Localized structures in a laser with a saturable absorber in a self-imaging resonator. *Phys. Rev. A*, 56:1582–1591, Aug 1997.

[13] Y. Tanguy, T. Ackemann, W. J. Firth, and R. Jäger. Realization of a semiconductor-based cavity soliton laser. *Phys. Rev. Lett.*, 100:013907, Jan 2008.

[14] P. Genevet, S. Barland, M. Giudici, and J. R. Tredicce. Cavity soliton laser based on mutually coupled semiconductor microresonators. *Phys. Rev. Lett.*, 101:123905, Sep 2008.

[15] T. Elsass, K. Gauthron, G. Beaudoin, I. Sagnes, R. Kuszelewicz, and S. Barbay. Fast manipulation of laser localized structures in a monolithic vertical cavity with saturable absorber. *Applied Physics B*, 98(2-3):327–331, 2010.

[16] P. Genevet, S. Barland, M. Giudici, and J. R. Tredicce. Bistable and addressable localized vortices in semiconductor lasers. *Phys. Rev. Lett.*, 104:223902, Jun 2010.

[17] P. Coullet, C. Riera, and C. Tresser. A new approach to data storage using localized structures. *Chaos*, 14:193–201, Mar 2004.

[18] M. Tlidi, P. Mandel, and R. Lefever. Localized structures and localized patterns in optical bistability. *Phys. Rev. Lett.*, 73:640–643, Aug 1994.

[19] N. N. Rosanov and G. V. Khodova. Autosolitons in bistable interferometers. *Opt. Spectrosc.*, 65:449, 1988.

[20] M. Brambilla, L. A. Lugiato, F. Prati, L. Spinelli, and W. J. Firth. Spatial soliton pixels in semiconductor devices. *Phys. Rev. Lett.*, 79:2042–2045, 1997.

[21] L.A. Lugiato. Introduction to the feature section on cavity solitons: An overview. *Quantum Electronics, IEEE Journal of*, 39(2):193–196, 2003.

[22] S. Barland, J. R. Tredicce, M. Brambilla, L. A. Lugiato, S. Balle, M. Giudici, T. Maggipinto, L. Spinelli, G. Tissoni, T. Knödl, M. Miller, and R. Jäger. Cavity solitons as pixels in semiconductor microcavities. *Nature*, 419(6908):699–702, Oct 2002.

[23] A.G. Vladimirov, A. S. Pimenov, and D. Rachinskii. Numerical study of dynamical regimes in a monolithic passively mode-locked semiconductor laser. *Quantum Electronics, IEEE Journal of*, 45(5):462–468, May 2009.

[24] A. G. Vladimirov, N. N. Rozanov, S. V. Fedorov, and G. V. Khodova. Bifurcation analysis of laser autosolitons. *Quantum Electronics*, 27(11):949, 1997.

[25] F. Leo, S. Coen, P. Kockaert, S.P. Gorza, P. Emplit, and M. Haelterman. Temporal cavity solitons in one-dimensional kerr media as bits in an all-optical buffer. *Nat Photon*, 4(7):471–476, Jul 2010.

[26] T. Herr, V. Brasch, J. D. Jost, C. Y. Wang, N. M. Kondratiev, M. L. Gorodetsky, and T. J. Kippenberg. Temporal solitons in optical microresonators. *Nature Photonics*, 8(2):145–152, 2014.

[27] Andrew Bao, Hualongand Cooper, Maxwell Rowley, Luigi Di Lauro, Juan Sebastian Totero Gongora, Sai T. Chu, Brent E. Little, Gian-Luca Oppo, Roberto Morandotti, David J. Moss, Benjamin Wetzel, Marco Peccianti, and Alessia. Pasquazi. Observation of mode-locked spatial laser solitons. *Nat. Photonics.*, 13:384–389, 2019.

[28] N. Englebert, C. Mas-Arabi, P. Parra-Rivas, S.P. Gorza, and F. Leo. Temporal solitons in a coherently driven active resonator. *Nat. Photonics.*, 15:536–541, 2021.

[29] M. Marconi, J. Javaloyes, S. Balle, and M. Giudici. How lasing localized structures evolve out of passive mode locking. *Phys. Rev. Lett.*, 112:223901, Jun 2014.

[30] M. Marconi, J. Javaloyes, P. Camelin, D.C. Gonzalez, S. Balle, and M. Giudici. Control and generation of localized pulses in passively mode-locked semiconductor lasers. *Selected Topics in Quantum Electronics, IEEE Journal of*, 21(6):1–10, Nov 2015.

[31] M. Marconi, J. Javaloyes, P. Camelin, D. Chaparro, S. Balle, and M. Giudici. Control and generation of localized pulses in passively mode-locked semiconductor lasers. *Selected Topics in Quantum Electronics, IEEE Journal of*, PP(99):1–1, 2015.

[32] Logan G. Wright, Demetrios N. Christodoulides, and Frank W. Wise. Spatiotemporal mode-locking in multimode fiber lasers. *Science*, 358(6359):94–97, 2017.

[33] Logan G. Wright, Pavel Sidorenko, Hamed Pourbeyram, Zachary M. Ziegler, Andrei Isichenko, Boris A. Malomed, Curtis R. Menyuk, Demetrios N. Christodoulides, and Frank W. Wise. Mechanisms of spatiotemporal mode-locking. *Nat. Phys.*, 16:565–270, 2020.

[34] F. Gustave, N. Radwell, C. McIntyre, J. P. Toomey, D. M. Kane, S. Barland, W. J. Firth, G.-L. Oppo, and T. Ackemann. Observation of mode-locked spatial laser solitons. *Phys. Rev. Lett.*, 118:044102, Jan 2017.

[35] Kyungduk Kim, Stefan Bittner, Yongquan Zeng, Stefano Guazzotti, Ortwin Hess, Qi Jie Wang, and Hui Cao. Massively parallel ultrafast random bit generation with a chip-scale laser. *Science*, 371(6532):948–952, 2021.

[36] F. Encinas-Sanz, Sonia Melle, and Oscar G. Calderón. Time-resolved dynamics of two-dimensional transverse patterns in broad area lasers. *Phys. Rev. Lett.*, 93:213904, Nov 2004.

[37] J. Javaloyes. Cavity light bullets in passively mode-locked semiconductor lasers. *Phys. Rev. Lett.*, 116:043901, Jan 2016.

[38] S. S. Gopalakrishnan, K. Panajotov, M. Taki, and M. Tlidi. Dissipative light bullets in kerr cavities: Multistability, clustering, and rogue waves. *Phys. Rev. Lett.*, 126:153902, Apr 2021.

[39] P. Camelin, C. Schelte, A. Verschelde, A. Garnache, G. Beaudoin, I. Sagnes, G. Huyet, J. Javaloyes, S.V. Gurevich, and M. Giudici. Temporal localized structures in mode-locked vertical external-cavity surface-emitting laser. *Optics Letters*, 43:5367, 2018.

[40] Y. Noblet and T. Ackemann. Analysis of spatial emission structures in vertical-cavity surface-emitting lasers with feedback from a volume bragg grating. *Phys. Rev. A*, 85:053812, May 2012.

[41] A. Laurain, M. Myara, G. Beaudoin, I. Sagnes, and A. Garnache. High power single–frequency continuously–tunable compact extended–cavity semiconductor laser. *Opt. Express*, 17(12):9503–9508, Jun 2009.

[42] A. Garnache, S. Hoogland, A.C. Tropper, I. Sagnes, G. Saint-Girons, and J. S. Roberts. Sub-500-fs soliton-like pulse in a passively mode-locked broadband surface-emitting laser with 100 mW average power. *Applied Physics Letters*, 80:3892–3894, 2002.

[43] P. Camelin, J. Javaloyes, M. Marconi, and M. Giudici. Electrical addressing and temporal tweezing of localized pulses in passively-mode-locked semiconductor lasers. *Phys. Rev. A*, 94:063854, Dec 2016.

[44] Q. Feng, J. V. Moloney, and A. C. Newell. Amplitude instabilities of transverse traveling waves in lasers. *Phys. Rev. Lett.*, 71:1705–1708, Sep 1993.

[45] Jan Hausen, Kathy Lüdge, Svetlana V. Gurevich, and Julien Javaloyes. How carrier memory enters the haus master equation of mode-locking. *Opt. Lett.*, 45(22):6210–6213, Nov 2020.

[46] S. V. Gurevich and J. Javaloyes. Spatial instabilities of light bullets in passively-mode-locked lasers. *Phys. Rev. A*, 96:023821, Aug 2017.

[47] G. New. Pulse evolution in mode-locked quasi-continuous lasers. *Quantum Electronics, IEEE Journal of*, 10(2):115 – 124, February 1974.

[48] N. N. Rosanov and G. V. Khodova. Autosolitons in nonlinear interferometers. *Opt. Spectrosc.*, 65:449–450, 1988.

[49] A. G. Vladimirov, S. V. Fedorov, N. A. Kaliteevskii, G. V. Khodova, and N. N. Rosanov. Numerical investigation of laser localized structures. *Journal of Optics B: Quantum and Semiclassical Optics*, 1(1):101, 1999.

[50] C. Palma and V. Bagini. Extension of the fresnel transform to abcd systems. *J. Opt. Soc. Am. A*, 14(8):1774–1779, Aug 1997.

[51] S. V. Fedorov, A. G. Vladimirov, G. V. Khodova, and N. N. Rosanov. Effect of frequency detunings and finite relaxation rates on laser localized structures. *Phys. Rev. E*, 61:5814–5824, May 2000.

[52] Hannes Uecker, Daniel Wetzel, and Jens D. M. Rademacher. pde2path - a matlab package for continuation and bifurcation in 2d elliptic systems. *Numerical Mathematics: Theory, Methods and Applications*, 7(1):58–106, 002 2014.

[53] Sandro M. Link, Alexander Klenner, Mario Mangold, Christian A. Zaugg, Matthias Golling, Bauke W. Tilma, and Ursula Keller. Dual-comb modelocked laser. *Opt. Express*, 23(5):5521–5531, Mar 2015.

[54] Sebastian Knitter, Changgeng Liu, Brandon Redding, Mustafa K. Khokha, Michael A. Choma, and Hui Cao. Coherence switching of a degenerate vecsel for multimodality imaging. *Optica*, 3(4):403–406, Apr 2016.

[55] C. Schelte, J. Javaloyes, and S. V. Gurevich. Dynamics of temporally localized states in passively mode-locked semiconductor lasers. *Phys. Rev. A*, 97:053820, May 2018.

[56] F. Pedaci, G. Tissoni, S. Barland, M. Giudici, and J. R. Tredicce. Mapping local defects of extended media using localized structures. *Appl. Phys. Lett.*, 93:111104, 2008.